ACADÉMIE
DES SCIENCES
INSTITUT DE FRANCE

Comptes Rendus

Géoscience

Sciences de la Planète

Alain Vauchez, Jean-Marie Dautria and Abdelkader El Maz

Natural deformation processes of lower crustal prismatic sillimanite under high to ultra-high temperature conditions highlighted by EBSD investigation

Volume 357 (2025), p. 555-566

Online since: 4 December 2025

https://doi.org/10.5802/crgeos.317

The Comptes Rendus. Géoscience — Sciences de la Planète *are a member of the Mersenne Center for open scientific publishing*
www.centre-mersenne.org — e-ISSN : 1778-7025

ACADÉMIE DES SCIENCES
INSTITUT DE FRANCE

Comptes Rendus. Géoscience — Sciences de la Planète
2025, Vol. 357, p. 555-566
https://doi.org/10.5802/crgeos.317

Research article
Petrology, petrophysics

Natural deformation processes of lower crustal prismatic sillimanite under high to ultra-high temperature conditions highlighted by EBSD investigation

Alain Vauchez [*, a], **Jean-Marie Dautria** [a] **and Abdelkader El Maz** [b]

[a] Geosciences Montpellier, Montpellier University and CNRS, 34095 Montpellier, France

[b] Department of Geology, University of Moulay Ismaïl, Meknes, Morocco

E-mail: alain.vauchez@umontpellier.fr (A. Vauchez)

Abstract. Quartzo-feldspathic and restitic granulites from the Middle Atlas lower crust (Morocco) contain prismatic sillimanite crystals up to 2 × 1 mm large, deformed under high temperature ($T \geq 850$ °C) and moderate pressure ($P \sim 0.9$ GPa) conditions. EBSD mapping reveals a heterogeneous deformation of sillimanite crystals in the quartzo-feldspathic samples depending on the minerals surrounding them. When they are included in sillimanite aggregates or constrained by large garnet grains, sillimanite deformation is strong and frequently reach dynamic recrystallization. Contrastingly, sillimanite crystals are significantly less deformed or even undeformed when isolated in the strongly deformed quartzo-feldspathic matrix. In the restitic samples almost all sillimanites display a homogeneous deformation but less frequent recrystallization. Deformed sillimanites display microstructures typical of dislocation-creep processes: misorientation, subgrain boundaries and subgrains, which point to recrystallization through subgrain rotation. Subgrain boundaries misorientation dominantly results from rotation around [100]. Crystallographic preferred orientation displays a concentration of [001] around the lineation. It is stronger in the restitic than in the quartzo-feldspathic samples, probably due to the heterogeneity of deformation in the latter. These data substantiate (010)[001] as the dominant dislocations slip system. This agrees with previous experimental deformation and transmission electron microscope observations. Our results differ from those obtained on fibrolitic sillimanite, which support (001)[010] and (001)[100] as dominant slip systems in large grains and a major effect of initial grain orientation relative to lineation. This difference may result from the contrasted P–T conditions of deformation: ≥850 °C and ~0.9 GPa for the Middle Atlas granulites, ~700 °C and ~0.45 GPa for the West Greenland ones.

Keywords. Prismatic sillimanite, High temperature, Deformation mechanisms, Dislocation creep, Dynamic recrystallization, Paragenesis control.

Manuscript received 15 July 2025, revised 15 October 2025, accepted 7 November 2025.

1. Introduction

Sillimanite is one of the three natural polymorphs of aluminosilicate ($Al_2O[SiO_4]$), the other two being andalusite and kyanite. It usually occurs in regional metamorphic rocks derived from Al-rich pelites and psammites or aluminous anatectic orthogneiss. More seldom, it may also appear in High Temperature (HT) hornfels (e.g., Deer et al., 2013). It is a nesosilicate which crystallizes in the orthorhombic

*Corresponding author

system and it occurs in two forms, either as bundles of undulating and twisted fine fibers, called fibrolites, or as slender elongated prisms with a nearly square basal section and a well-marked cleavage parallel to {010}. The shape of sillimanite crystals depends on the crystallization conditions, but in all case, this mineral is an indicator of high-temperature metamorphism. The fibrolite variety occurs in metamorphic rocks at the upper limit of medium-grade amphibolite facies (e.g., Guidotti, 1970). The prismatic variety characterizes rocks belonging to HT to UHT granulitic facies. As shown in Suzuki et al. (2025, Figure 12), in such conditions, sillimanite can crystallize during prograde evolution (e.g., through the breakdown of muscovite+quartz) and retrograde one (through the breakdown of garnet; e.g., Kerrick, 1987; El Maz and Guiraud, 2001; Guidotti and Johnson, 2002).

In a recent paper (El Maz, Vauchez, et al., 2025), we described a set of prismatic sillimanite-bearing quartzo-feldspathic and refractory metapelitic granulite xenoliths from a Moroccan Quaternary tuff ring (Tafraoute, 33°31′29″N–4°41′35″W, 550 Ka) which belongs to the Middle Atlas alkaline volcanic district. The setting of the collected xenoliths has been previously described in details in El Messbahi, Bodinier, et al. (2015) and El Messbahi, Dautria, et al. (2020) and El Maz, Vauchez, et al. (2025). In addition to their richness in prismatic sillimanite (up to more than 50% in the case of some refractory samples) whose size reaches 2 mm long and 1 mm wide, these granulites contain garnet, orthopyroxene, spinel, ilmenite, rutile, osumilite and corundum are also present but in very minor amounts. The El Maz, Vauchez, et al. (ibid.) thermobarometric study of quartzo-feldspathic granulites supports that the lower crust of Middle Atlas underwent several successive metamorphic episodes. P–T conditions of the first event (1.1 ± 0.1 GPa and 850–880 °C), likely hercynian, were estimated in sample G3, selected for the present study, using the composition of feldspars included in garnet and of the garnet core. Then, temperature and pressure estimated using the Opx-Grt geothermobarometer for Opx of coronas in contact with the rims of garnets substantiate a progressive heating up to ultra-high Temperatures ($T = 1050 \pm 50$ °C) under relatively moderate Pressure ($P = 0.9 \pm 0.1$ GPa) that triggered anhydrous partial melting. At the beginning of this heating, responsible for the formation of prismatic sillimanites, the lower crust underwent a transtensional deformation likely responsible for the deformation of sillimanites (ibid.). In addition, temperatures between 720 and 830 °C have been estimated from the exchange of Ca, Na and K between plagioclase and K-feldspars in the matrix of quartzo-feldspathic samples. These lower temperatures likely correspond to post-alpine cooling before the extraction of the xenoliths during the volcanic episode. The sillimanite prisms from these granulites are more or less deformed depending on the samples and their large sizes make observation and study of this deformation with optic microscope and Electron BackScattered Diffraction (EBSD) rather easy.

Sillimanite-bearing samples from various geodynamic contexts have been studied. In most of them, prismatic sillimanite did not recorded post-crystallization deformation. Therefore, only few studies have been carried to characterize the deformation mechanisms of this mineral. Among them, Doukhan and Christie (1982) experimentally deformed monocrystals of prismatic sillimanite under temperature of 900 °C, pressure of 1.1 GPa, and strain rate of 10^{-5} s^{-1} and studied the deformed prisms in a Transmission Electron Microscope (TEM). They concluded that [001] glides in (100) and (010) are the easiest glide systems, even if the deformed samples were cut with an orientation that favor activation of the [100](010) and [010](100) slip systems. In 1990, Lambregts and Van Roermund published a detailed TEM study of prismatic sillimanite from South Norway, deformed under P–T conditions of 0.6 GPa and 750 °C. They showed that under such conditions, prismatic sillimanite deforms plastically with (100)[00l] being the dominant and (001)[l00] the subordinate slip-systems. More recently, Piazolo and Jaconelli (2014), using the EBSD techniques, published a detailed study of fibrolitic sillimanite deformation mechanisms in an Archean paragneiss from southern West Greenland deformed at ~700 °C and ~0.45 GPa. They showed that the (001)[010] and (001)[100] slip systems are dominant and that (010)[001] and (100)[001] are also activated in needles initially oriented with [001] parallel to the lineation. They also concluded that grain boundary sliding was activated and was dominant in the outer parts of fine-grained clusters.

Our study provides new data on natural deformation of prismatic sillimanite under HT to UHT

conditions. They can be compared to the results of experimental deformation of Doukhan and Christie (1982) as well as those of TEM studies of monocrystals (e.g., Lambregts and Van Roermund, 1990). Our data are statistically better representative of the deformation of this mineral at the rock scale. They also allow to consider the effect of the surrounding mineral paragenesis on the behavior of prismatic sillimanite crystals. The recent improvements of the EBSD technique and of data processing, especially using the MTEX toolbox in MATLAB (Hielscher and Schaeben, 2008; Bachmann et al., 2010; Bachmann et al., 2011; Mainprice et al., 2014, https://mtex-toolbox.github.io/) allowed us to better determine crystallographic orientations including those of tiny grains and also intracrystalline misorientations and associated microstrucures. In addition, we can compare dominant deformation mechanisms of prismatic sillimanite at high temperature with those of fibrolitic sillimanite at lower temperature revealed by Piazolo and Jaconelli (2014).

2. Methodology

Among the samples described in El Maz, Vauchez, et al. (2025), we have selected two sillimanite-rich granulites for detailed study of the sillimanite deformation mechanisms using Electron Backscattered Diffraction (EBSD): one quartzo-feldspatic (G3) and one quartz and feldspar free restitic (TAF501). The size of sample G3 (~75 cm long) allowed to accurately determine the macroscopic lineation and foliation; then to cut two well-oriented thin sections, the first one (G3xz) parallel to the lineation (X structural axis) and to the pole to foliation plane (Z structural axis), i.e., in the XZ structural plane, and the second (G3yz) perpendicular to the lineation, i.e., in the YZ structural plane. For the refractory TAF501, the foliation and lineation were more difficult to recognize and only one thin section was cut almost in the XZ plane.

After detailed observation under the optical microscope, carefully polished thin sections of these samples have been analyzed using the EBSD technique for detailed crystallographic mapping and measurements to characterize intracrystalline microstructures and mechanisms active during deformation. Indexing of EBSD patterns was performed in a Camscan Crystal Probe X500FE scanning electron microscope (Geosciences Montpellier, University of Montpellier, France) equipped with EBSD and energy dispersive spectroscopy (EDS) detectors, both controlled by the AZtecHKL acquisition software (Oxford Instruments). Acquisition of diffraction patterns was performed with a working distance of 25 mm and an acceleration voltage of 18 to 21 kV. To map the whole thin sections, we use a grid step size of 10 μm for the two G3 and 15 μm for TAF501. The two detailed maps on G3xz and G3yz were performed with a grid step size of 5 μm and 4 μm respectively. These last step sizes have been chosen to obtain a precise description of all crystals, including the smallest ones, and of their internal structure. The raw indexation rate varies from 75% to 82%. To improve the indexation rate and rebuilt more crystals, we processed raw data using Channel 5 software (Oxford Instruments) and the MTEX toolbox in MATLAB (http://mtex-toolbox.github.io/, Hielscher and Schaeben, 2008; Bachmann et al., 2010; Bachmann et al., 2011; Mainprice et al., 2014) following the procedure described in detail in Baptiste et al. (2015). With MTEX, we also computed the orientation distribution functions (ODFs) using the "de la Vallée Poussin" kernel function (half-width of 10°), the Crystallographic Preferred Orientation (CPO) and intragranular misorientations parameters for sillimanite. These misorientations result essentially from the accumulation of geometrically necessary dislocations; they were quantified using the Kernel Average Misorientation (KAM, a measure of the mean misorientation around a measured pixel) and the local misorientation relative to the mean orientation of the grain (Mis2Mean).

3. Microstructures

Detailed mineralogical and phases chemical composition of both G3 and TAF501 were published in El Maz, Vauchez, et al. (2025). Figure 1 shows the EBSD maps of the whole studied thin sections. In addition to prismatic sillimanite, only major phases that may have influenced its deformation are considered in this section.

Both studied samples contain prismatic sillimanites up to 2 mm long. In TAF501, most of them display subgrain boundaries and only few are partially recrystallized while, in G3, a larger proportion of sillimanite crystals are partially to totally recrystallized.

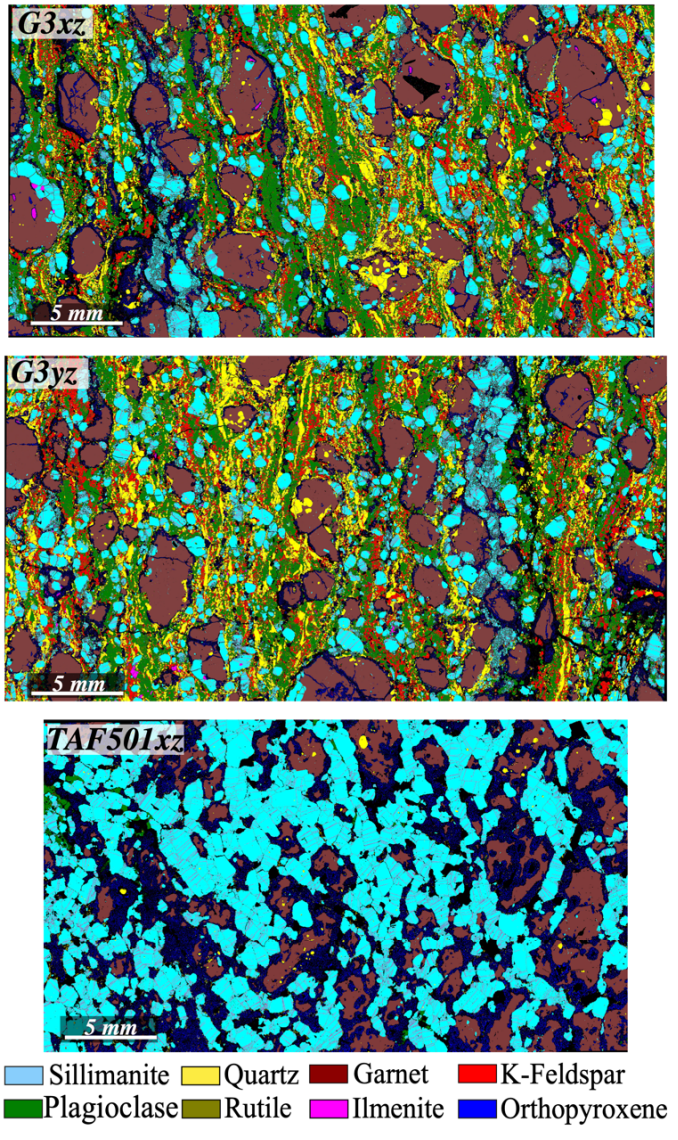

Figure 1. EBSD maps of the three thin sections used in this study to determine deformation mechanisms in prismatic sillimanite. G3 is representative of the quartzo-feldspatic granulites and TAF501 of the restitic ones. Each color corresponds to a mineral phase (color chart under the maps) except the black color that identifies not-indexed pixels. Light purple lines inside sillimanite crystals (aqua blue) represent subgrain boundaries. The grid step size is 10 μm for G3xz and G3yz and 15 μm for TAF501. Better quality images are available as Figures S1–S3 in Supplementary material.

The G3 microstructure in both sections (G3xz and G3yz, Figure 1) is heterogeneous, especially garnets and sillimanites display local concentrations in layers elongated parallel to the foliation. In addition, plagioclase form monomineralic narrow layers (up to 1 mm thick) in which grains display re-equilibrated boundaries with straight segments and 120° triple junctions. These plagioclase layers alternate with fine-grained quartz layers (0.1 to 0.4 mm thick) that contain many elongate rectangular crystals (platten-quartz). Fine-grained K-feldspar is more dispersed through the thin sections and some grains display

interstitial shape or form films between grains of other phases. In both planes, garnet shape is ovoid with its maximum length parallel to the direction of the foliation. The garnet size is slightly smaller in the YZ (up to 5×3 mm) than in the XZ (up to 6×4 mm) planes. All crystals are surrounded by narrow coronas constituted of undeformed tiny grains of Opx ± spinel. In both G3xz and G3yz, sillimanite is dispersed through the rock but it locally forms aggregates preferentially associated with garnet. In G3xz, the shape of most sillimanite crystals (up to 2×1 mm) is elongated parallel to the lineation with an ovoid tendency (Figure 1). These crystals display intracrystalline misorientations associated to subgrain boundaries perpendicular to their elongation. However, a small proportion of sillimanite crystals isolated in the quartzo-feldspathic matrix have a rather rounded shape and are free of subgrain boundaries (Figures 2 and S4 Supplementary material). In G3yz (Figure 1), sillimanite crystals shape is less elongate and rather smaller than in G3xz. In addition, the orientation of elongated crystals is more dispersed, and they display subgrain boundaries and a clear intracrystalline misorientation. In both thin sections, sillimanite crystals, either incorporated in monomineralic aggregates or in garnet-sillimanite aggregates, are partially to totally recrystallized (Figure 2). The new grains have a size between ~20 and ~80 μm and an angular equidimensional shape, except in some places where they are slightly elongated parallel to the foliation (Figure 2).

Sample TAF501 (Figure 1, TAF501xz) is almost entirely constituted of garnet and sillimanite. Most garnets are elongated (up to ~1 cm long and 0.4 cm wide), but their long axis is frequently slightly oblique to the lineation. All garnet crystals are more or less disrupted and they are wrapped by Opx ± spinel coronas resulting from garnet breakdown, which are significantly larger than in G3. At the thin section scale sillimanite crystals are jointed and forms a kind of network including garnets and their Opx coronas (Figure 1). The sillimanite crystals shape tends to be rectangular with a larger size than in G3 (up to 2.5 mm) and a long axis parallel to the lineation, except when they wrap large garnets. Almost all crystals of sillimanite contain well-developed subgrain boundaries and only few of them are partially recrystallized (Figure 1).

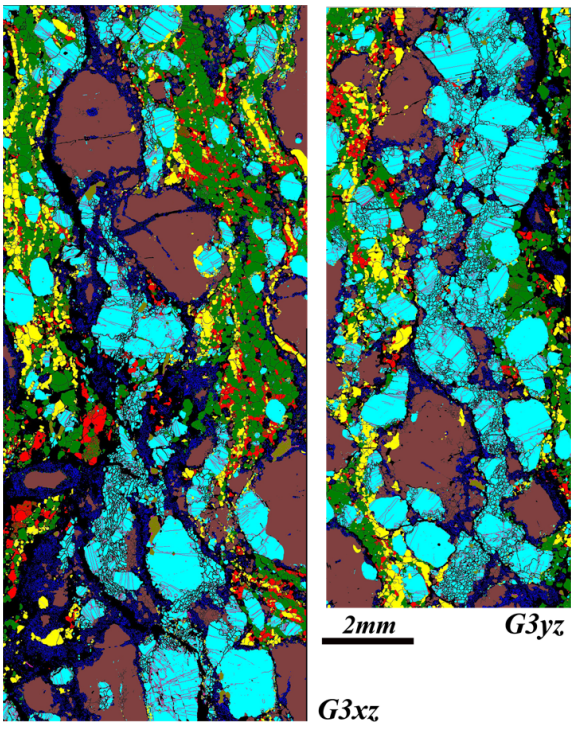

Figure 2. Detailed EBSD maps of two areas of concentration of partially recrystallized prismatic sillimanite (aqua) and garnet (brown) partly replaced by Opx (dark blue) **in** both the G3xz and G3yz thin sections. The grid step size is 5 μm for G3xz and 4 μm for G3yz. The color chart is the same as in Figure 1.

4. Crystallographic preferred orientations and intracrystalline misorientations

The crystallographic preferred orientations of samples G3 and TAF501 are rather similar (Figure 3): they are characterized by a clear, but not strong concentration of [001] parallel to the lineation and a dispersion of [100] and [010] within and around the YZ structural plane, with weak concentrations of both axis around the pole of the foliation (Z structural axis). In TAF501, the concentration of [100] is significantly stronger than the [010] one. This suggests that (100)[001] was the dominant slip system in TAF501 while in G3 the CPO favors an equivalent activation of both (100)[001] and (010)[001] slip systems.

The CPOs measured in the detailed maps of Figure 2 are less informative (Figure 4). The statistics are

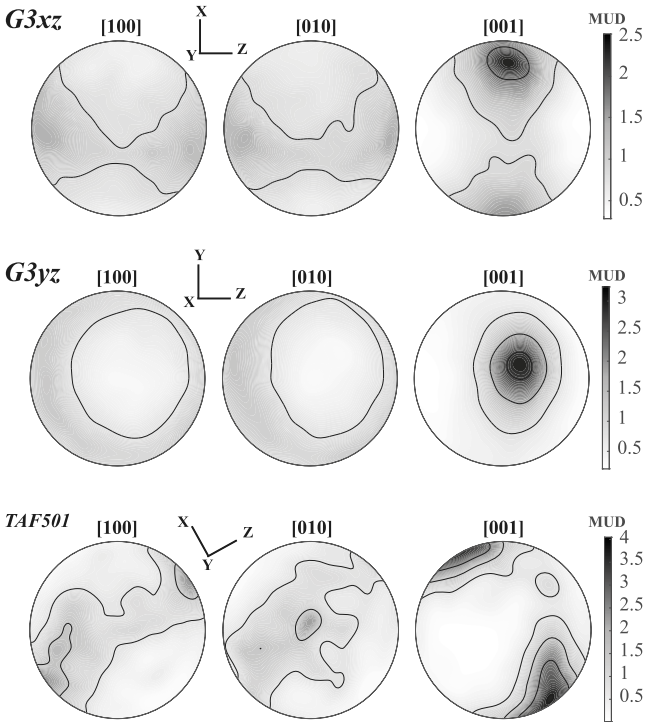

Figure 3. Sillimanite crystallographic preferred orientation from EBSD measurements on the three thin sections. Lower-hemisphere stereographic projections of one mean orientation per grain with contours at multiple of a uniform distribution (MUD). Both samples display a clear, although not strong, concentration of [001] parallel to the lineation.

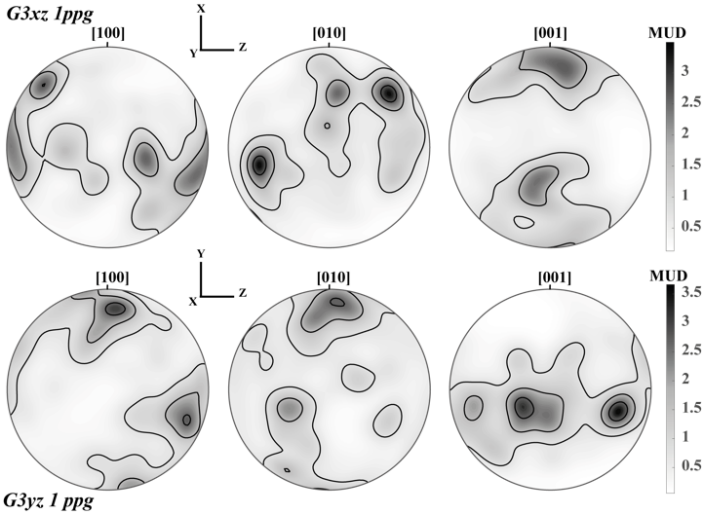

Figure 4. Crystallographic preferred orientation of sillimanite from the strongly recrystallized domains shown on Figure 2. These CPO are more dispersed than those obtained for the whole thin section; this dispersion is probably due to dynamic recrystallization. Similar projection and contours characteristics than in Figure 3. 1 ppg = One point per grain, i.e., an average orientation was plotted for each grain.

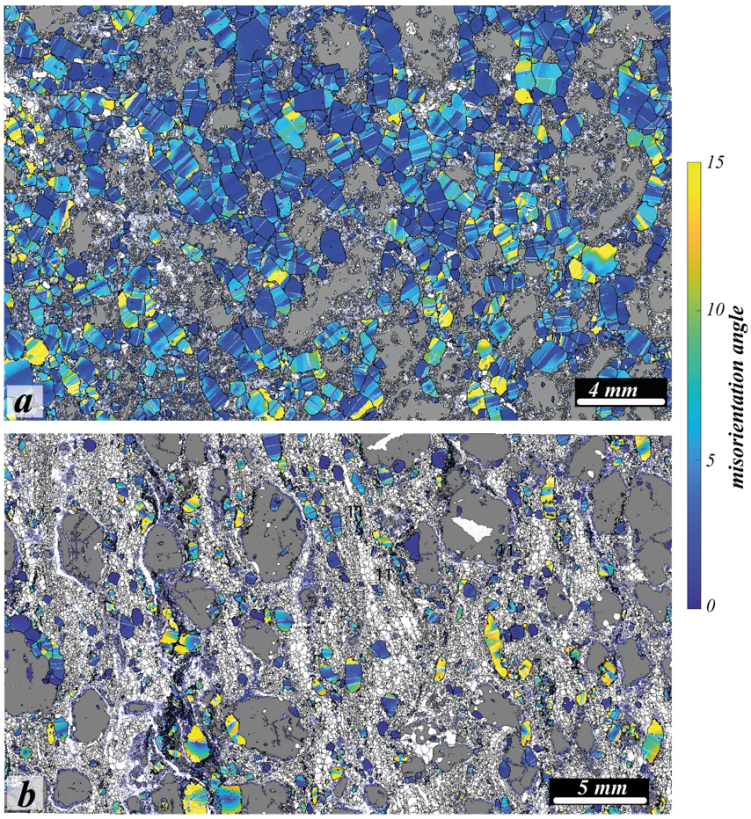

Figure 5. Miss2Mean map of sillimanite in samples TAF501 (a) and G3xz (b). The variation of color represents the misorientation of each measured point inside a crystal relative to the crystal mean orientation. The misorientation between subgrains is up to ~15°. The white lines limiting color variations inside sillimanite crystals are subgrain boundaries. In TAF501, almost all grains display subgrains domains with a variation of orientation up to 15°. In G3xz, grains isolated in the quartzo-feldspathic matrix display only weak or even no intragranular misorientation. Grey color is Garnet and white is the color of all other minerals.

perturbated by either the big size of porphyroclasts relative to the new grains one when plotted with the whole measurements in each grain, or by the large number of new grains recrystallized from the same parent grain when plotted with one mean value per grain (one point per grain). However, these CPOs illustrate a dispersion of the crystallographic axes' orientation, inclusive of [001], but [001] and [100] are the only axes showing a concentration around the *X* and the *Z* structural axes respectively.

Detailed mapping of intragranular crystallographic orientation (step of 5 and 4 μm) reveal intragranular misorientations, their organization and their intensity. For instance, Figure 5 (and S5) shows the misorientations associated to subgrain boundaries and the misorientation angle up to ~15° relative to the mean orientation of the grain (Miss2Mean map) in samples TAF501 and G3xz. Interestingly, the CPO in G3xz is slightly weaker than in TAF501, although more sillimanite grains have been partially to totally dynamically recrystallized than in TAF501. In the latter almost all sillimanite crystals display subgrain boundaries and rather strong intragranular misorientation while in G3, a significant proportion of sillimanite grains are isolated in the quartzo-feldspathic matrix and most of them only display a faint or even no deformation. This heterogeneity may have dispersed the CPO in G3 and explain why its fabric is weaker than the TAF501 one.

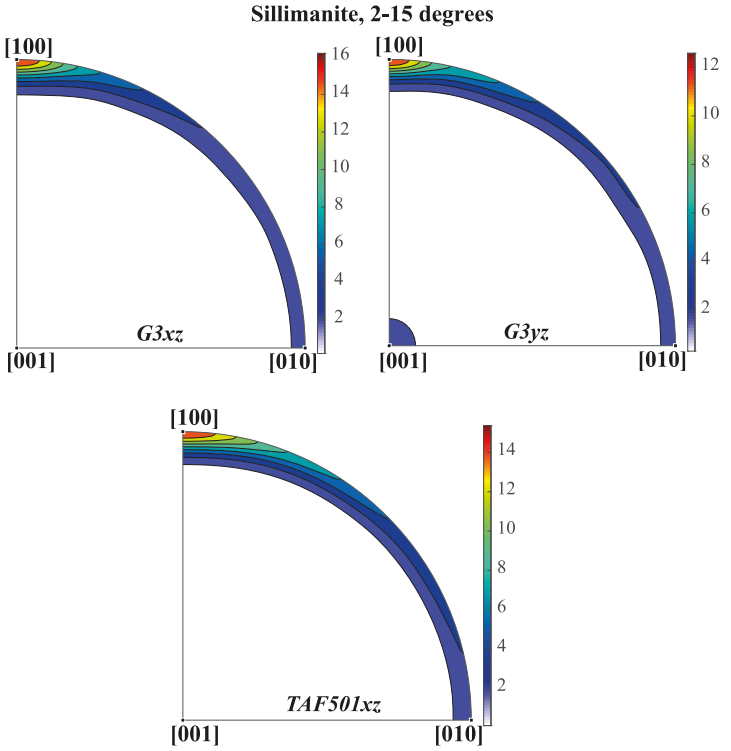

Figure 6. Crystallographic orientation of the rotation axes for misorientations between 2 and 15° in G3xz and TAF501. Both samples display a strong concentration of rotation axes around [100] and a few ones parallel to [010] and none around [001]. This supports that the main slip direction of dislocation was [001].

In the three thin sections (Figure 6), a large majority of misorientation axis with rotation in the range 2°–15° (subgrain boundaries) are parallel or close to [100] and only a minority to [010]. These subgrain boundaries are perpendicular to both the slip plane and the slip direction, thus, combined with the CPO (Figure 3) this supports that the dominant slip system is (010)[001] and that (100)[001] is a subsidiary one.

Partially recrystallized sillimanites frequently display subgrain boundaries that progressively become new grain boundary (Figure 7). In several sillimanite grains, a few subgrain boundaries are predominantly orthogonal or less frequently oblique to the main (001) ones. These different systems interact to form small subgrains of similar size than the new grains (Figure 7). The misorientation axes of these subgrain boundaries are frequently [010] or [100]. This points to the participation of subsidiary slip systems with [100] or [010] slip directions to the recrystallization process.

5. Discussion and conclusions

Data and observations obtained from the Middle Atlas lower crustal granulites using the EBSD technique strengthen the determination of the dominant processes active in prismatic sillimanite during natural deformation under high temperature conditions (≥850 °C). Deformation of prismatic sillimanite crystals in the studied granulites is characterized by intragranular microstructures (subgrains boundaries to subgrains) typical of dislocations creep leading to recrystallization by subgrains rotation. Most subgrains boundaries have misorientation axis parallel or close to [100].

The dominant slip systems during the deformation of the studied prismatic sillimanite, statistically determined from EBSD data, are (010)[001] and (100)[001]. They are similar to those evidenced by TEM characterization carried out on single-crystals experimentally deformed (Doukhan and Christie,

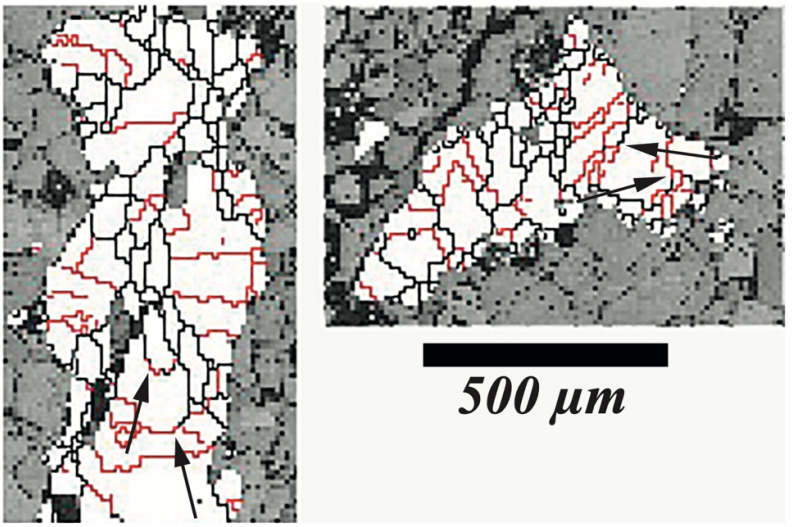

Figure 7. Excerpts from KAM maps of sample G3 showing the intracrystalline structure of two partially recrystallized sillimanite grains. Black lines are grain boundaries (misorientation >15°) and red ones are subgrain boundaries (misorientation of 2°–15°). These maps display examples of progressive transition from subgrain boundary to grain boundary (e.g., arrow on both images).

1982) and on naturally deformed garnet-migmatite (Lambregts and Van Roermund, 1990). Interestingly, EBSD mapping of the G3yz thin section shows that many crystals of sillimanite are elongate obliquely or less frequently perpendicularly to the foliation. In addition, they display subgrain boundaries perpendicular to [001] with [100] as main misorientation rotation axis. This supports that they deformed through dislocation creep with [001] as dominant slip direction. Some of them, initially misoriented relatively to the deformation axes, were still deformed mostly through dislocation glide parallel to [001], suggesting a flattening strain component in addition to dominant shearing. The behavior of these crystals agrees with Doukhan and Christie (1982) observations that even initially misoriented grains deformed through dislocations creep parallel to [001].

In contrast with prismatic sillimanites, in the fibrolite sillimanites studied by Piazolo and Jaconelli (2014), the slip systems (001)[010] and (001)[100] are dominant, at the exception of needles that were initially oriented with [001] parallel to the lineation, and for which [001] is the main slip direction. This difference may result from several causes in addition to the initial orientation of sillimanite crystals relative to the lineation. The most likely are the P–T conditions under which deformation occurred: ~700 °C and 0.45 GPa, in the biotite stability field, for the fibrolites studied by Piazolo and Jaconelli (ibid.), versus >850 °C and ~1 GPa, outside the biotite stability field, for the Middle Atlas prismatic sillimanites. In the first case, the three slip systems may be equally activated depending on the initial orientation of the crystals when, under higher temperature conditions, the [001] slip direction is more easily activated than the other two and become largely dominant. However, an effect of the strain regime cannot be ruled out since deformation occurred through simple shear for the fibrolites (ibid.) versus transtensional shear for the Middle Atlas granulites.

EBSD data from the quartzo-feldspathic granulite G3 highlight that the deformation of sillimanite is highly heterogeneous depending on the nature of the minerals surrounding the sillimanite crystals (Figures 8, 5 and S2). Deformation is stronger when sillimanite grains are surrounded by either other sillimanites or garnet or both. In these cases, deformation may extend to dynamic recrystallization. In contrast, sillimanite grains isolated in the quartzofeldspatic matrix are less deformed or even escaped deformation, even those that were well oriented for

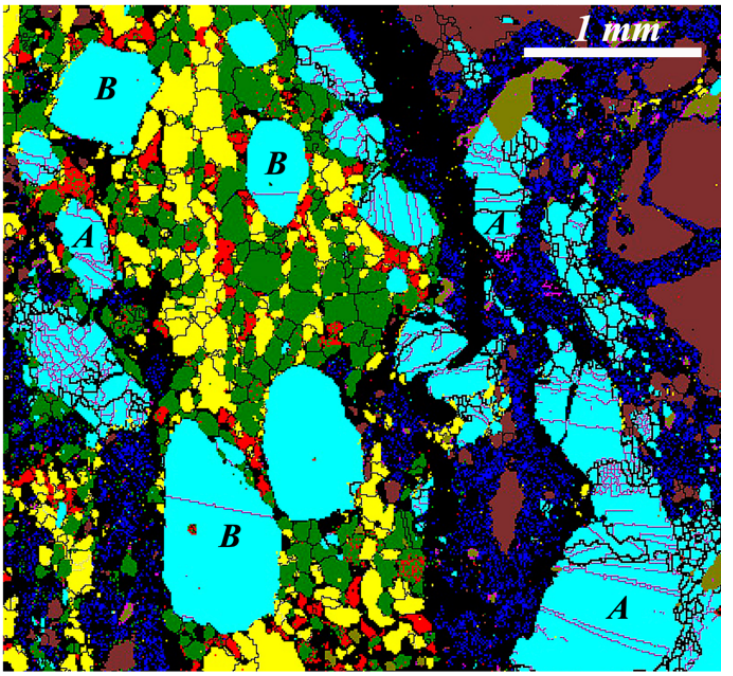

Figure 8. Detail from the EBSD map of G3xz thin section showing an example of the contrast of deformation between sillimanite involved in an aggregate of garnet and sillimanite (e.g., *A*) and sillimanite grains surrounded by quartz and plagioclase (e.g., *B*). Black lines are grain boundaries and purple ones are subgrain boundaries (misorientation <15°). The color chart is the same than on Figure 1.

the dominant slip systems to be activated. Comparing in G3 the microstructures of sillimanite with those of surrounding quartz and plagioclase highlights that under high temperature conditions prismatic sillimanite is stiffer than quartz and feldspars and, thus, may have escaped deformation because strain was fully accommodated by the quartzo-feldspathic matrix.

In the restitic granulite TAF501, only few sillimanite crystals are partially recrystallized. Almost all sillimanite grains display transverse subgrain boundaries that limit subgrains generally displaying moderate misorientation. This suggests that dislocations climb and associated recovery of the crystal lattice in the subgrains were active during deformation. The restitic sample TAF501 and the quartzo-feldspathic G3 display contrasted characteristics: the deformation of sillimanite crystals is more homogeneous and weaker in the first one and only few grains are partially recrystallized while, in the second one, it is more heterogeneous and locally strong enough to trigger full recrystallization. However, the CPO of TAF501 is paradoxically stronger than the G3 one. This is likely related to their mineralogical compositions, the restitic granulites are almost entirely composed of garnet and sillimanite and deformation was more homogeneously distributed than in the quartzo-feldspathic ones in which a large proportion of sillimanite grains are dispersed in more deformable quartzo-feldspatic layers that accommodated the deformation that did not, or only slightly, affected sillimanite crystals.

A remaining question is “During which stage of the studied granulites evolution did the deformation of prismatic sillimanites occur?”. Several convergent microstructural observations described in more details in El Maz, Vauchez, et al. (2025) allow to provide a reliable answer. The destabilization coronas around garnets do not display evidence of a significant deformation, even when they are in contact with strongly deformed sillimanites. The microstructures inside the coronas are well preserved although these aggregates of very small grains of orthopyroxene and spinel are rather easy to deform. The temperature of

garnet destabilization was estimated at 1050 ± 50 °C using Opx and garnet thermobarometers. The quartzo-feldspathic granulites, G3 for instance (Figure 1), contain interstitial crystals of quartz, K-feldspars and, more seldom plagioclase, related to an episode of anhydrous partial melting that occurred at the peak temperature. These crystals have retained their interstitial habitus and do not display any evidence of post crystallization deformation. In G3, platten-quartz are present in monomineralic layers between sillimanites. Such quartz grains, typical of static annealing under HT conditions and slow cooling, do not display evidence of subsequent deformation. These structural characteristics all together support that: (1) the deformation of sillimanite occurred before garnet destabilization, i.e., during the prograde stage of the metamorphic evolution of the studied granulites, and (2) in the quartzo-feldspathic granulites (e.g., G3), the formation of platten-quartz, the crystallization of interstitial grains, and the subsequent cooling occurred under static conditions, so after sillimanite deformation. No evidence of significant deformation during the retrograde stage of the metamorphic evolution has been detected. This led El Maz, Vauchez, et al. (ibid.) to consider that the deformation of the prismatic sillimanites occurred at the beginning of the episode of heating to UHT responsible for the destabilization of garnet and the anhydrous partial melting.

Finally, the studied deformed prismatic sillimanites, especially in sample G3, have only recorded an incipient post-deformation annealing, although they have been submitted to ultra-high temperatures after deformation (ibid.). This points to the high thermal stability of their crystallographic structure, even under temperature around 1000 °C (e.g., Holland and Carpenter, 1986; Igami et al., 2017).

Acknowledgements

We warmly acknowledge Doriane Delmas and Christophe Nevado for the preparation of high-quality polished thin sections, Fabrice Barou for the time devoted to the acquisition of high-grade EBSD data, Andrea Tommasi for her support during the processing and interpretation of EBSD data. We thank the anonymous reviewer for her/his suggestions that helped us to improve our manuscript. We also thank Houssa Ouali and Hicham El Messbahi for their help during samples collection.

Declaration of interests

The authors do not work for, advise, own shares in, or receive funds from any organization that could benefit from this article, and have declared no affiliations other than their research organizations.

Supplementary materials

Supporting information for this article is available on the journal's website under https://doi.org/10.5802/crgeos.317 or from the author.

References

Bachmann, F., R. Hielscher and H. Schaeben, "Texture analysis with MTEX- free and open source software toolbox", *Sol. State Phenom.* **160** (2010), pp. 63–68.

Bachmann, F., R. Hielscher and H. Schaeben, "Grain detection from 2D and 3D EBSD data-specification of the MTEX algorithm", *Ultramicroscopy* **111** (2011), pp. 1720–1733.

Baptiste, V., A. Tommasi, A. Vauchez, S. Demouchy and R. L. Rudnick, "Deformation, hydration, and anisotropy of the lithospheric mantle in an active rift: constraints from mantle xenoliths from the North Tanzanian Divergence of the East African Rift", *Tectonophysics* **639** (2015), pp. 34–55.

Deer, W. A., R. A. Howie and J. Zussman, *An Introduction to the Rock-forming Minerals*, 3rd edition, The Mineralogical Society: London, 2013.

Doukhan, J. C. and J. M. Christie, "Plastic deformation of sillimanite Al_2SiO_5 single crystals under confining pressure and TEM investigation of the induced defect structure", *Bull. Minéral.* **105** (1982), no. 6, pp. 583–589. Online at https://www.persee.fr/doc/bulmi_0180-9210_1982_num_105_6_7638.

El Maz, A. and M. Guiraud, "Paragenèse à faible variance dans les métapélites de la série de Filali (Rif interne marocain) : description, interprétation et conséquence géodynamique", *Bull. Soc. Géol. Fr.* **172** (2001), no. 4, pp. 469–485.

El Maz, A., A. Vauchez and J. M. Dautria, "Post-Hercynian ultrahigh-temperature tectono-metamorphic evolution of the Middle Atlas lower crust (central Morocco) revealed by metapelitic granulite xenoliths", *Solid Earth* **16** (2025), pp. 1–22.

El Messbahi, H., J. L. Bodinier, A. Vauchez, J. M. Dautria, H. Ouali and C. Garido, "Short wavelength lateral variability of lithospheric mantle beneath the Middle Atlas (Morocco) as recorded by mantle xenoliths", *Tectonophysics* **650** (2015), pp. 34–52.

El Messbahi, H., J. M. Dautria, H. Jourde, P. Münch, O. Alard and H. Ouali, "Eruption dynamics of pleistocene maars and tuff rings from the Azrou-Timahdite district (Middle Atlas, northern Morocco) and its relevance to environmental changes and ground water table characteristics", *J. Afr. Earth Sci.* **167** (2020), article no. 103845.

Guidotti, C. V., "The mineralogy and petrology of the transition from the lower to upper sillimanite zone in the Oquossoc Area, Maine", *J. Petrol.* **11** (1970), no. 2, pp. 277–336.

Guidotti, C. V. and S. E. Johnson, "Pseudomorphs and associated microstructuresof western Maine, USA", *J. Struct. Geol.* **24** (2002), pp. 1139–1156.

Hielscher, R. and H. Schaeben, "A novel pole figure inversion method: specification of the MTEX algorithm", *J. Appl. Crystallogr.* **41** (2008), pp. 1024–1037.

Holland, T. and M. Carpenter, "Aluminium/silicon disordering and melting in sillimanite at high pressures", *Nature* **320** (1986), pp. 151–153.

Igami, Y., S. Ohi and A. Miyake, "Sillimanite-mullite transformation observed in synchrotron X-ray diffraction experiments", *J. Am. Ceram. Soc.* **100** (2017), no. 10, pp. 4928–4937.

Kerrick, D. M., "Fibrolite in contact aureoles of Donegal, Ireland", *Am. Mineral.* **72** (1987), no. 3–4, pp. 240–254.

Lambregts, P. J. and H. L. M. Van Roermund, "Deformation and recrystallization mechanisms in naturally deformed sillimanites", *Tectonophysics* **179** (1990), no. 3–4, pp. 371–378.

Mainprice, D., F. Bachmann, R. Hielscher and H. Schaeben, "Descriptive tools for the analysis of texture projects with large datasets using MTEX: strength, symmetry and components", *Geol. Soc. Spec. Publ.* **409** (2014), pp. 251–271.

Piazolo, S. and P. Jaconelli, "Sillimanite deformation mechanisms within a grt-sil-bt gneiss: effect of pre-deformation grain orientations and characteristics on mechanism, slip-system activation and rheology", *Geol. Soc. Spec. Publ.* **394** (2014), pp. 189–213.

Suzuki, K., T. Kawakami, T. Kogiso, S. Sakata, F. Higashino, M. Yokoi and S. Kudo, "Tectonic setting and evolution of anatectic melt composition during prograde metamorphism up to UHT metamorphism: Constraints from *P*–*T*–*t* melting path from Rundvågshetta, Lützow–Holm Complex, East Antarctica", *J. Metamorph. Geol.* **43** (2025), pp. 467–495.